

Ordered SMSI Decoration Layer on Rh Nanoparticles Grown on TiO₂(110) Surface

Z. Majzik,^{§,†} N. Balázs,[‡] and A. Berkó*,[‡]

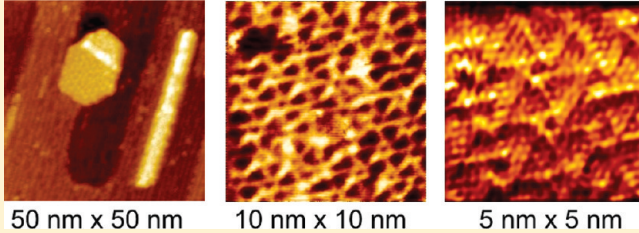
[†]Department of Physical Chemistry and Material Science, University of Szeged, Szeged, Hungary

[‡]Reaction Kinetics Laboratory, Institute of Nanochemistry and Catalysis, Chemical Research Center of the Hungarian Academy of Sciences, P.O. Box 168, H-6701 Szeged, Hungary

 Supporting Information

ABSTRACT: Rh nanoparticles of 20–40 nm lateral size were grown on TiO₂(110) surface by physical vapor deposition and thermal treatments. The top-facet morphology of the Rh nanoparticles and the particle-free support were characterized by scanning tunneling microscopy. The chemical composition of the surface was checked by Auger electron spectrometry. Although most of the particles exhibited complex overlayers, ordered decoration layers were detected only on the top facet of extended hexagonal Rh particles. Several ordered or quasi-ordered encapsulation phases were detected: (1) a “worm-like” overlayer consisting of 1D stripes (width of 0.5 nm and length of 2–3 nm) oriented in the close-packed crystallographic orientations of the Rh nanoparticles and (2) a “wheel-like” hexagonal structure with unit cell vectors of 1.50 (± 0.05) nm. The “worm-like” structure is suggested to be an initial stage in the formation of a “wheel-like” structure. It was proved that it is possible to selectively remove the “wheel-like” decoration phase by Ar⁺ sputtering and to recover it by thermal treatment of a few minutes at 1000 K.

ordered decoration phase on Rh nanocrystallites grown on TiO₂(110)



50 nm x 50 nm 10 nm x 10 nm 5 nm x 5 nm

and the “wheel-like” structure is suggested to be an initial stage in the formation of a “wheel-like” structure. It was proved that it is possible to selectively remove the “wheel-like” decoration phase by Ar⁺ sputtering and to recover it by thermal treatment of a few minutes at 1000 K.

1. INTRODUCTION

The almost half-century effort for deeper understanding of the so-called strong metal–support interaction (SMSI) exhibits several turning points: (1) the detection of this phenomenon (SMSI state) appeared as the effect of an appropriate thermal treatment of noble metals supported on reducible oxides in a reductive atmosphere¹ and the connection of this state to a strongly suppressed CO chemisorption ability of the catalysts;^{2,3} (2) the observation that this state appears also in vacuum as the effect of annealing at high temperatures (600–1000 K), depending on the defect concentration in the bulk of the support oxide;^{2–4} (3) the justification that the CO uptake on extended metal surfaces is determined by a simple site-blocking effect in which the coverage of the decoration oxide is proportional to the inhibited amount of adsorbed carbon-monoxide;⁵ (4) the statement that this feature can be explained mainly by surface diffusion of oxygen-deficient phases of the reducible support onto the top of noble metal nanoparticles⁴ or by formation of surface alloy or alloy oxides;^{2,6} (5) demonstration of the self-limiting nature and the lateral ordering of the decoration layers detected on metal nanoparticles supported by oxide single crystal surfaces (2D model catalyst).^{6–8}

It was recognized that the ordered ultrathin epitaxial oxide layers of different stoichiometries can serve as an excellent model system for the oxide-supported catalysts.^{9,10} In the present state of affairs, the biggest challenge is to explore all possible ordered decoration layers and to find connection between these structures

and their chemical composition. The research devoted to this aim is carried out in two different ways: (1) epitaxial growth of oxide ultrathin films on metal single crystal surfaces as a function of oxidation conditions, listed here without a claim of completeness for TiO_x/metal single crystal systems: Pt(111),^{11–15} Pt(110)–(1 × 2),¹⁶ Pt(100),^{17,18} Ru(0001),¹⁹ Rh(111),⁵ Cu(100),^{20,21} Ni(110),^{22–25} Au(111),²⁶ Re(10T0),²⁷ Mo(112),^{28,29} Mo(100),³⁰ Mo(110),^{31,32} W(110),³³ W(100);^{34,35} (2) detection of ordered encapsulation phases on noble metal nanoparticles such as Pt^{7,8} and Pd⁶ supported on oxide single crystals. Although much effort has been made in the first direction by low-energy electron diffraction measurements, the real breakthrough was made by the application of scanning tunneling microscopy. For the studies in the second direction, scanning tunneling microscopy (STM) is the most appropriate method and is able to detect ordered phases on the surface of individual nanocrystallites. In addition to some previous works^{3,4,36} presenting suggestions on the mechanism of the decoration process, this phenomenon was recently reviewed by Fu and Wagner, and a more complete theory was given for its driving force.³⁷ In their model operating with the Schottky barrier formed at the particle/support interface, it was successfully explained why certain metals supported on reducible oxides exhibit decoration phenomenon.

Received: November 29, 2010

Revised: April 6, 2011

Published: April 26, 2011

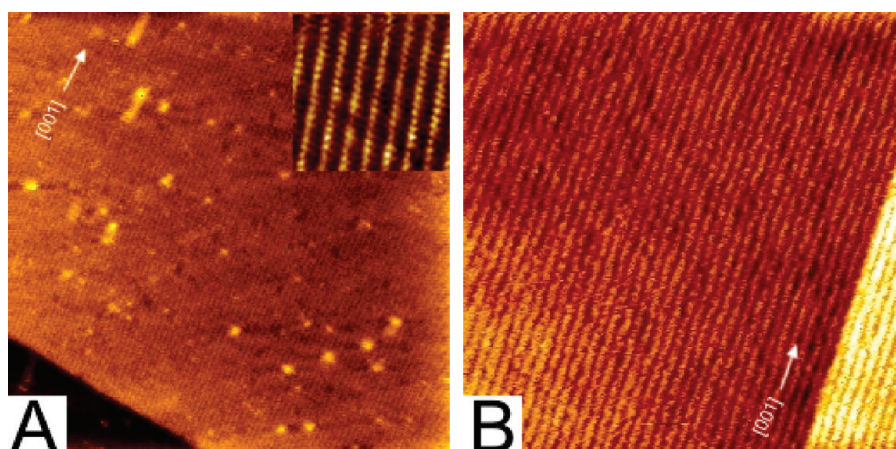


Figure 1. Characteristic STM cc images of $50 \times 50 \text{ nm}^2$ recorded on (A) $\text{TiO}_2(110)$ -(1 \times 1) and (B) $\text{TiO}_2(110)$ -(1 \times 2) surfaces used as support in this work. Insert in Figure 1A: atomically resolved STM ch image of $5 \times 5 \text{ nm}^2$.

In the present work, ordered and quasi-ordered TiO_x phases formed on the top facets of Rh crystallites supported on a $\text{TiO}_2(110)$ surface are investigated by STM. Moreover, the effect of soft Ar^+ bombardment and restoration of the decoration layer by thermal treatments are evaluated in the light of the proposed structure of the decoration layer.

2. EXPERIMENTAL SECTION

The experiments were carried out in an ultrahigh vacuum (UHV) system evacuated down to 5×10^{-8} Pa and equipped with a commercial room temperature (RT) scanning tunneling microscope (WA-Technology, Cambridge, U.K.), a cylindrical mirror analyzer with a central electron gun (Staib Instruments, Langenbach, Germany) and a quadrupole mass spectrometer (Balzers-Pfeiffer, Aslara, Germany). Note that in this work, MS technique was applied only for checking the gas phase composition.

STM images of 256×256 pixels were generally recorded in constant current mode at a sample bias of $+1.5$ V on the sample and a tunneling current of 0.1 nA. Both W and Pt-Ir tips were applied in the course of the experiments, and no substantial difference was experienced for these materials. The constant current (cc) morphology images are shown in top-view representation, where brighter areas correspond to higher Z (or tunneling current, I_t) values. Images of enhanced lateral resolution were recorded in constant height (ch) mode (current images), where the position-dependent variation of tunneling current served for constructing the image. In the case of some images of high lateral resolution, a gentle FFT treatment was also applied. The $X-Y-Z$ calibration of the STM images was performed by measuring the characteristic morphological parameters of the $\text{TiO}_2(110)$ -(1 \times 1) support (lateral unit cell, $0.31 \text{ nm} \times 0.65 \text{ nm}$; height of the steps,³⁶ 0.32 nm). A careful tip conditioning was applied in the course of the measurements to obtain reliable particle sizes. This procedure contained not only coarse and fine bias-pulse treatments, but also an extended in situ “annealing” of the tip end at 180 V and 100 nA in feedback mode for 10 – 20 min.

One side epi-polished $\text{TiO}_2(110)$ single crystal of $5 \times 5 \times 1 \text{ mm}^3$ was directly fixed to a Ta filament (in some cases, to a Si plate) by an oxide adhesive (ceramobond-571, Aremco Products, Valley Cottage, NY), and it was mounted on a transferable sample holder. The probe was indirectly annealed by the current flowing through the Ta filament or the Si plate. The temperature of the probe was measured

by a chromel—alumel (K-type) thermocouple stuck to the side of the sample by the same oxide adhesive. It is worth noting that we have never detected any contamination due to these components, even after extended high-temperature thermal treatments of the probe. The cleaning of the sample was started by a gradual increase of the temperature up to 1050 K, and it was continued by Ar^+ bombardment at 1000 K with step-wise decreased ion energies of 2 , 1.5 , and 1 keV and an average current density of 4 – $6 \mu\text{A}/\text{cm}^2$ for 1 – 2 h. This procedure not only resulted in the purification of the sample and getting rid of Ca and K contamination but also caused some reduction in the subsurface layer, resulting in a more conductive sample (beneficial for avoiding charging effect during spectroscopy and microscopy measurements). To reset the TiO_2 stoichiometry, the samples were from time to time reoxidized in 5×10^{-2} Pa oxygen for 20 min at 900 K. The final treatment was usually a short annealing at 1050 K in UHV. For the measurements presented in this work, a bulk-terminated (1 \times 1) surface decorated by 0D dot and 1D stripes (reduced Ti_2O_3 phase) of low concentration and almost completely reconstructed TiO_2 -(1 \times 2) surfaces were applied.

Rh was deposited by a commercial four-pocket evaporator (Oxford Applied Research, Oxford, U.K.) in which a high-purity (99.95%) Rh rod served as a metal source. The surface concentration of the deposited Rh was estimated from the volume of the nanoparticles. The metal coverage is expressed in monolayer equivalents (ML) by taking into account the atom density of the $\text{Rh}(111)$ surface ($1.60 \times 10^{15} \text{ Rh atom}/\text{cm}^2$) and a layer-to-layer distance of 0.22 nm .

3. RESULTS

3.1. Tailored Formation of Rh Crystallites on $\text{TiO}_2(110)$ Surface.

Regarding the support oxide, it is well-known that the actual surface morphology of a TiO_2 single crystal is sensitively affected by the former treatments of the probe.³⁶ This behavior correlates with the oxidation state of the subsurface layers that gradually varies due to treatments such as Ar ion sputtering or annealing at higher temperatures (>800 K). This change also reveals itself in the apparent color of the sample, from transparent to dark blue. Most of the experiments presented here were carried out on a bulk-terminated $\text{TiO}_2(110)$ -(1 \times 1) surface exhibiting defect features of low concentration.³⁸ Figure 1A shows an STM

image of cc mode ($50 \times 50 \text{ nm}^2$) recorded in a region of typical morphology. The inserted ch mode image ($5 \times 5 \text{ nm}^2$) exhibits rows separated by 0.65 nm. We also used more reduced samples having a complete (1×2) reconstruction.³⁹ In the case of the (1×1) surface, the bright dots can be identified with 5-fold Ti^{4+} ions. For a (1×2) arranged surface, however, the bright rows belong to one-dimensional Ti_2O_3 added rows of [001] orientation separated by 1.30 nm (Figure 1B). Note that the different ordered and quasi-ordered $\text{TiO}_2(110)$ surfaces were characterized in detail in several previous papers and reviews.³⁶

Regarding the supported metal particles, to detect the inner structure of the top facets, one needs nanoparticles. Three distinct methods were applied in this work to form larger Rh particles: (1) deposition of Rh at RT and annealing at elevated temperatures, (2) deposition of Rh at elevated temperatures in the range of 850–1050 K, and (3) deposition of Rh at elevated temperature (1050 K) onto a $\text{TiO}_2(110)$ surface previously decorated with Rh nanoparticles. In the first case, the average size of the particles will be rather low as compared with those prepared by the other two methods. Nevertheless, by depositing a larger amount of Rh (8–10 ML), the first method leads to the formation of larger dendrite-like nanoparticles. By applying the second and third methods, the deposition performed at high temperatures results in the growth of large and well-separated Rh particles.^{40,41}

Figure 2 displays some characteristic STM images recorded after different deposition conditions. The deposition of 0.03 ML of Rh at 330 K onto a $\text{TiO}_2(110)$ - (1×2) surface and annealing at 850 K for 10 min results in 1–2 atomic layer thick Rh nanoparticles with a diameter of $\sim 1.5 \text{ nm}$ (Figure 2A). The size of the image is $20 \times 20 \text{ nm}^2$, and the average particle density is $\sim 1.5 \times 10^{12} \text{ cm}^{-2}$. It can be seen that the particles preferentially occupy the bright rows identified with a reduced 1D phase (Ti_2O_3), and some of them are slightly elongated along the rows. Despite the appearance of somewhat elongated Rh particles in the first step, the Rh particles postgrown at 850 K (deposition of an additional 0.25 ML Rh onto the surface characterized in Figure 2A) are mostly of round shape (Figure 2B). The average diameter and thickness of the nanoparticles varied in the range of $\sim 1.5\text{--}2.2 \text{ nm}$ and 1–3 atomic layers, respectively. The particle density (the number of particles on a unit surface area) did not change, suggesting that the mean free path of the atomic diffusion is larger than the average particle–particle distance ($\sim 4\text{--}6 \text{ nm}$) in the present case.

The same sequence of experiments was also performed at 950 K (instead of 850 K, before) (Figure 2C, D). The size of these latter STM images is $50 \times 50 \text{ nm}^2$. It can be observed that nearly round Rh nanoparticles are formed after the deposition of Rh (0.05 ML) at 330 K and annealing of the probe at 950 K for 10 min (Figure 2C). The average diameter of these nanoparticles is 3 nm, and they consist of 2–3 atomic layers. The postdeposition of Rh at 950 K results in mainly elongated particles, independently of their location (Figure 2D). Note that some pits around the particles appear frequently, as can be seen at the end of the nanoparticle located on the right terrace of the recorded region. The appearance of similar features indicates clearly that the titania surface itself becomes mobile above 900–950 K.⁴² At the same time, the change in the growth mode, in which the formation of elongated particles will be prevailing, is probably connected with the activation of the support lattice diffusion, as well. On the basis of a more detailed investigation of the 1D growth of Rh particles, we can state that the ratio of the elongated and the round particles increases gradually by raising the temperature in the range of 850–1050 K. Moreover, this behavior is more or less independent

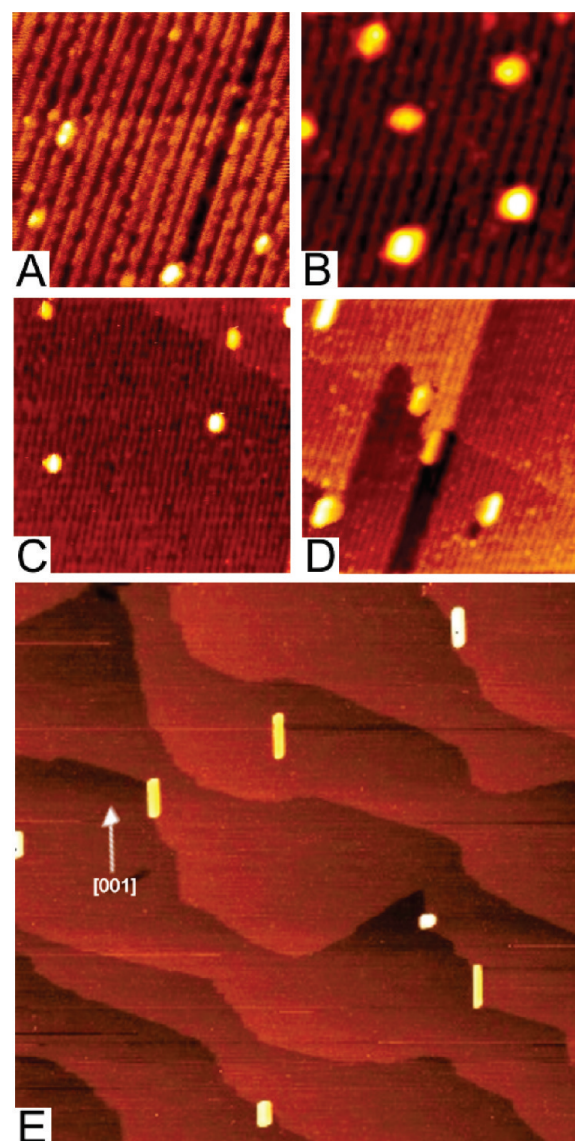


Figure 2. The morphology of $\text{Rh}/\text{TiO}_2(110)$ - (1×2) surfaces prepared by different treatments and detected by STM in cc mode: (A) deposition of 0.03 ML of Rh at 330 K, followed by 10 min annealing at 850 K; (B) after deposition of additional 0.25 ML Rh at 850 K onto the surface imaged in part A; (C) deposition of 0.05 ML of Rh at 330 K, followed by 10 min annealing at 950 K; (D) after deposition of an additional 0.30 ML Rh at 950 K onto the surface imaged in part C. Image sizes: (A, B) $20 \times 20 \text{ nm}^2$, (C, D) $50 \times 50 \text{ nm}^2$. (E) STM image of $400 \times 400 \text{ nm}^2$ recorded on $\text{TiO}_2(110)$ - (1×1) deposited by Rh (0.30 ML) at 1050 K.

of the reconstruction of the support; it appears also on a bulk-terminated $\text{TiO}_2(110)$ - (1×1) surface. Strongly elongated Rh nanoparticles were formed at high probability after the deposition of Rh at 1050 K (without seeding before) onto an unreconstructed titania surface, as is shown in a large-scale STM image of $400 \times 400 \text{ nm}$ (Figure 2E).

The main message of the experimental results presented in this section is that by varying the deposition conditions, it is possible to grow isotropically or anisotropically extended Rh nanoparticles, which provides facility for detailed and systematic study of the formation of SMSI decoration films. The detection and analysis of the ordered or quasi-ordered decoration layers formed

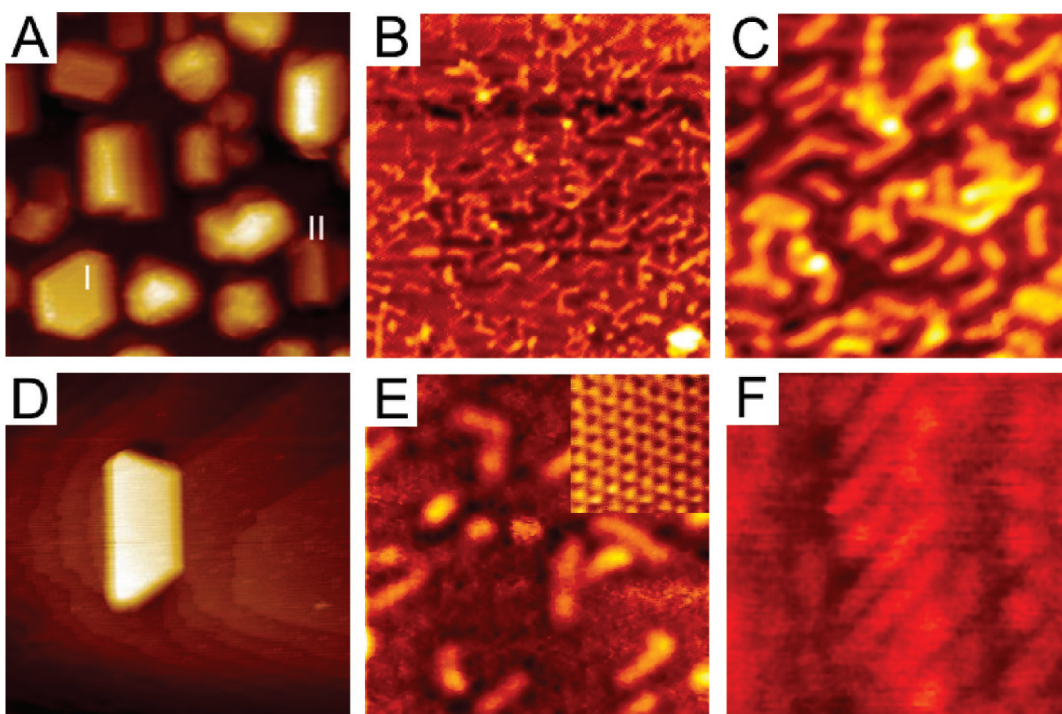


Figure 3. Worm-like decoration layer detected on different Rh nanoparticles supported on a $\text{TiO}_2(110)$ - (1×2) surface. (A) Large Rh particles grown by a postgrowth method on $\text{TiO}_2(110)$ - (1×2) surface at 1050 K ($200 \times 200 \text{ nm}^2$). (B, C) STM ch images recorded on the top facet of a hexagonal Rh particle, indicated by I on the cc image (A). Image sizes: (B) $20 \times 20 \text{ nm}^2$ and (C) $100 \times 100 \text{ nm}^2$. (D) Large elongated hexagonal Rh nanoparticle detected on a $100 \times 100 \text{ nm}^2$ area and (E) its top facet structure (the inset shows a $2 \times 2 \text{ nm}^2$ area of clean Rh in atomic resolution). (F) Periodic overlayer structure observed on the top facet of an elongated nanoparticle indicated by II in the image (A). The size of the latter image is $5 \times 5 \text{ nm}^2$. The STM images (D, E, F) were recorded in cc mode.

in the growth procedures described above are reported in the subsequent part of this work. The terminology used in a recent study on a TiO_x film/Pt(111) system presented by Granozzi et al. was applied for similar structures observed in this work.^{13,14}

3.2. "Worm-Like" Decoration Layer. Formation of a quasi-ordered decoration layer was observed for giant hexagonal particles, indicated by I in Figure 3A. These particles were grown by postgrowth of Rh on a $\text{TiO}_2(110)$ - (1×1) surface: deposition of 0.8 ML Rh at 1050 K followed by a repeated deposition of 10 ML of Rh at 1050 K. The size of the image is $200 \times 200 \text{ nm}^2$. Note that due to the tip–particle convolution, it was difficult to obtain a sharp perimeter line around the particles. The height of this nanoparticle is $\sim 2.5 \text{ nm}$ (10–12 atomic layers). The constant-height STM images of two different scales of $20 \times 20 \text{ nm}^2$ and $10 \times 10 \text{ nm}^2$ in Figure 3B and C recorded on its top facet clearly show the appearance of 1D stripes with a length of 2–3 nm and a width of $\sim 0.5 \text{ nm}$. These features are randomly oriented in a hexagonal overall structure, which is probably determined by the symmetry of Rh(111) facet. They are more or less uniformly distributed on the Rh facet (Figure 3B), and a few of them follow the edge of the particle aligned in the [001] orientation of the support oxide. This structure is reminiscent of a "worm-like" texture also described by Sedona et al.;¹³ however, in our case, it clearly consists of straight 1D nanostripes. A very similar overlayer structure but with a lower concentration of the stripes was detected on the top facet of the postgrown elongated and hexagonal Rh nanoparticle shown in Figure 3D. In this case, in addition to the stripes, some 0D nanodots can also be seen in the image of $10 \times 10 \text{ nm}^2$ (Figure 3E). Moreover, an atomically resolved image of the undecorated facet regions clearly exhibits

a configuration characteristic of the Rh(111) surface with a periodicity of $0.27 (\pm 0.01) \text{ nm}$ (the bulk nearest distance is 0.269 nm), as can be seen in the inset of $2 \times 2 \text{ nm}^2$ (Figure 3E). The decoration layer detected on a 14 atomic layer high elongated Rh nanoparticle (indicated by II on the Figure 3A) exhibits periodically arranged stripes with a separation of 0.53 nm , being very close to the (1×2) periodicity (Figure 3 F). The size of the latter STM image is $5 \times 5 \text{ nm}^2$.

All the STM images presented in this section were recorded in constant current mode by chemically etched W-tip. The subsequent high-resolution images, however, were recorded mostly in constant height mode to obtain the best lateral contrast.

3.3. "Wheel-Like" Decoration Layer. Our first experimental indication of a 2-dimensional long-range ordered encapsulation layer was obtained on large hexagonal Rh crystallites grown by deposition of Rh ($\sim 1.2 \text{ ML}$) at 1050 K onto a Rh-seeded (deposition of 0.04 ML Rh at 300 K, followed by annealing at 1050 K for 15 min) $\text{TiO}_2(110)$ - (1×2) sample. Figure 4A shows a $50 \times 50 \text{ nm}^2$ region where both a hexagonal and an elongated Rh particle can be seen. The top facet of both particles exhibits some extra features, suggesting the formation of decoration phase. In the case of the hexagonal crystallite, the dots are arranged in a quasi-hexagonal ordering, as is presented in a magnified image of $6 \times 6 \text{ nm}^2$ (Figure 4B). These images were recorded in constant current mode. As indicated in Figure 4A, there is a rotation angle of $17 (\pm 2)^\circ$ between one edge of the hexagonal crystallite and one row of their overlayer structure.

In another case, in which the Rh particles were grown on a $\text{TiO}_2(110)$ - (1×1) surface (without preseeding) by deposition of 0.8 ML Rh at 1050 K (Figure 4C), a less intense hexagonal

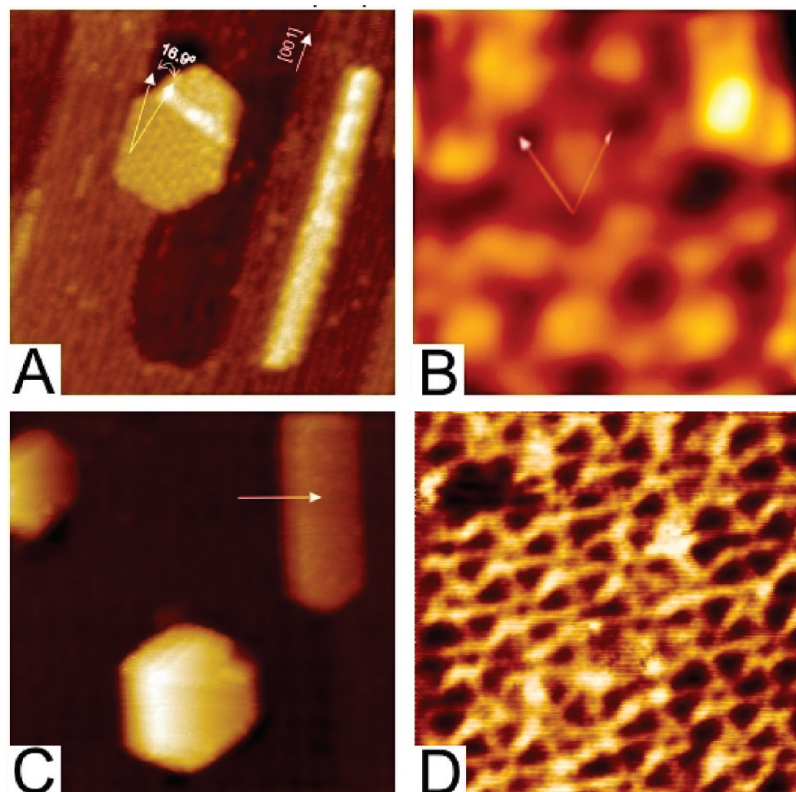


Figure 4. (A) Hexagonal and elongated Rh nanoparticles grown on $\text{TiO}_2(110)$ surface exhibiting 1D reduced Ti_2O_3 phase in high concentration. (B) The top facet of the hexagonal particle indicating the presence of quasi-ordered hexagonal decoration layer. (C) STM image showing large Rh particles and (D) its long-range ordered decoration phase (wheel structure). Image sizes: (A, C) $50 \times 50 \text{ nm}^2$, (B, D) $6 \times 6 \text{ nm}^2$. Images A, B, and C were recorded in cc mode; image D was detected in ch mode.

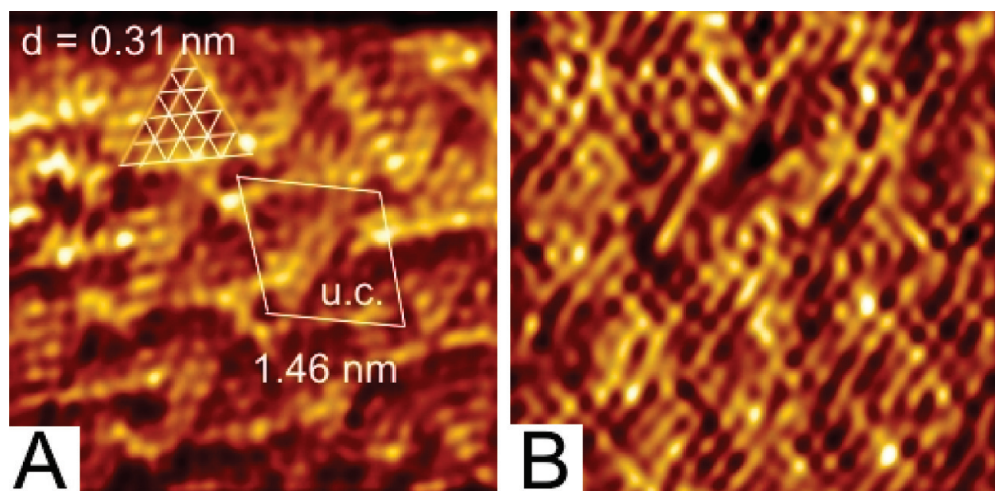


Figure 5. (A, B) Atomically resolved constant height STM images detected on a completely decorated large, hexagonal Rh particle formed at 1050 K. They show the wheel structure in two different contrasts. The characteristic lattice parameters are indicated on the image (A). Image sizes: $5 \times 5 \text{ nm}^2$.

wheel structure was recorded in constant height mode, as shown in Figure 4D. This texture was detected on the top facet of an elongated particle (a 5–6 atomic layers height nanoplank) indicated by the arrow in Figure 4C. The periodicity of the hexagonally arranged wheel structure was $1.50 (\pm 0.05) \text{ nm}$, determined by the average distance of the pivots (black holes in the center of the wheels).

It is worth noting that the top facets of the hexagonal particles are not always parallel to the plane of the support oxide, but they can show a typical declination of $8\text{--}10^\circ$, as in the case of the center bottom particle in Figure 4C. This declination angle can be explained by the formation of a reconstructed $\text{TiO}_2(110) // \text{Rh}(111)$ interface at the early stage of the Rh nucleation. Nevertheless, for the detection of ordered decoration layers,

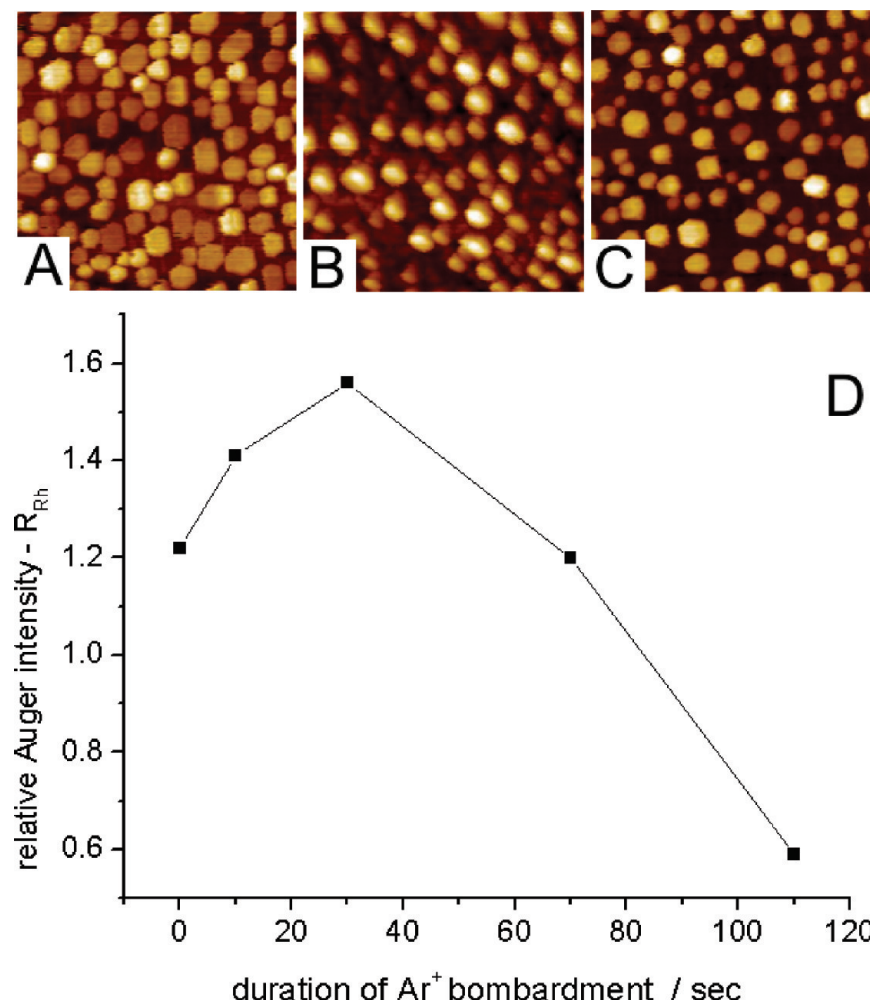


Figure 6. STM and AES detection of the removal of Rh nanoparticles formed at 1050 K. STM images of $100 \times 100 \text{ nm}^2$ detected (A) before and (B) after 110 s Ar^+ bombardment at room temperature and (C) following 10 min annealing at 1050 K in UHV. (D) Change in the relative intensity of Rh (302 eV) and Ti (385 eV) AES signals as a function of the duration of Ar^+ sputtering.

we chose the particles with the top facet parallel to the substrate, indicating the $\text{TiO}_2(110)/(1 \times 2)$ interface.

To improve the resolution of the imaging of encapsulation layers, we used constant height mode. In the course of recording the image, both the current and the bias were carefully adjusted. In Figure 5, two STM ch images recorded with different imaging parameters and contrasts are presented on a more or less completely ordered encapsulation layer. The hexagonal unit cell ($1.46 \pm 0.05 \text{ nm}$) of this periodic structure can be clearly recognized, as indicated in Figure 5A. Note that the unit cell of this structure is slightly smaller than that of the similar pattern in Figure 4. One side of the bright triangles of the wheel structure exhibits a rotation angle of 11° , compared with one of the unit cell vectors. The inner atomic structure is also appreciable, and it clearly consists of six atoms (5 times the 0.31 nm atom-to-atom distance) in the direction of the wings. The atomic rows are more visible in Figure 5B, although the contrast for the wheel structure itself is reduced in this case.

3.4. Removing and Restitution of Decoration Layers by Ar^+ Sputtering at Room Temperature and Subsequent Annealing in Vacuum. In the subsequent experiments, we chose a preparation method that results in Rh crystallites with rather large top facets. The surface morphology detected by STM after

depositing 13 ML of Rh at room temperature and annealing the $\text{TiO}_2(110)-(1 \times 2)$ sample at 1050 K for 5 min is shown in Figure 6A. The size of the selected characteristic region was $100 \times 100 \text{ nm}^2$, and the surface density of the particles was $\sim 0.97(\pm 0.05) \times 10^{12} \text{ cm}^{-2}$. The largest hexagonal particles consist of 25–30 atomic layers. Starting from this state, the effect of stepwise Ar^+ bombardment ($\sim 12 \mu\text{A}/\text{cm}^2$, 0.5 keV) on the relative Auger electron spectrometry (AES) intensity of Rh (R_{Rh}) is shown in Figure 6D. R_{Rh} is defined as the ratio between the peak-to-peak intensity on dN/dE Auger-spectra for Rh and Ti elements at energies of 302 and 385 eV, respectively. This value increases in the first period of the bombardment (~ 0 –30 s) from ~ 1.2 up to 1.6, followed by a gradual decrease down to 0.6 at 110 s duration of the sputtering. The initial increase in the Rh signal has already been observed by similar AES and low-energy ion scattering spectroscopy measurements, and it was explained by the removal of a TiO_x decoration ultrathin film from the top of the supported and encapsulated metal nanoparticles.⁴

After accomplishing the sputtering cycles, the surface morphology was tested by STM (Figure 6B). The characteristic surface area of $100 \times 100 \text{ nm}^2$ exhibits similar surface density of the nanoparticles, with significantly modified shape (unfortunately, this special image is also influenced by a tip-shape convolution

effect). The sharp, hexagonal outline of the particles disappeared, and the average corrugation of the surface decreased by $\sim 40\%$. An estimation for the removed amount of Rh was possible by recording STM images after 5 min annealing at 1050 K (Figure 6C). The hexagonal morphology of the separated Rh particles is recovered. The Rh coverage was ~ 6 ML, and the surface density of the particles was $\sim 0.95 (\pm 0.05) \times 10^{12} \text{ cm}^{-2}$. The highest particles consist of 20–25 atomic layers (only slightly less than originally), indicating that the Ar^+ sputtering and annealing reduce mainly the mean diameter of the nanoparticles. From the decrease in coverage for the states of A and C (Figure 6), it can be estimated that in our case, 15–20 s sputtering is sufficient for removing 1 ML of Rh. We assume that this statement is also valid for the encapsulation layer.

In the following experiments, we investigate the restitution of the ordered encapsulation layer removed previously by Ar^+ sputtering. After cleaning the $\text{TiO}_2(110)$ surface and preparing Rh particles similarly as above, the sample was sputtered for only 20 s, at which point the relative AES signal for Rh reached roughly a maximum (Figure 7A). Subsequently, the probe was stepwise annealed up to elevated temperatures, and after each annealing cycle, an AES spectra was recorded (Figure 7B). There is a slight ($\sim 10\%$) decrease in R_{Rh} resulting from the effect of annealing between 300 and 450 K, followed by a range (450–800 K) of almost constant level. The initial decrease at low temperatures may be explained by reordering of the Rh nanocrystallites; however, regarding the increased mobility of the support material due to the previous ion sputtering, a limited decoration process cannot also be excluded in this low temperature range. The reordering of the surface Rh means that atomically dispersed Rh produced by the ion bombardment can condense on the larger Rh nanoparticles.

For the thermal treatments in the range between 800 and 1000 K, the decrease in Rh relative the AES ratio is very pronounced, and it reaches a value that is slightly lower than that before the Ar^+ bombardment (Figure 7B). The difference between the final value of R_{Rh} (1.0) in Figure 7B and its initial value (1.34) in Figure 7A is larger than the error limit of the measurement; accordingly, it indicates the removal of some amount of Rh itself, or it suggests a modified stoichiometry or some contamination of the bar support regions. Nevertheless, the main drop in the R_{Rh} signal between 800 and 1000 K is probably a consequence of the recovery and the shadowing effect of the decoration TiO_x thin film. It means that for our samples, the formation of a decoration film takes place in the temperature range of 800–1000 K, as can be seen in the STM images (Figure 7C–F). The constant height images of $4 \times 4 \text{ nm}^2$ clearly show that the wheel structure is present before the sputtering (Figure 7C), but obviously disappears after the bombardment and annealing at 650 K in UHV for 5 min (Figure 7D). Some ordering can be observed after the thermal treatment at 900 K for 5 min (Figure 7E), but the reappearance of triangles characteristic of the wheel structure takes place only after annealing at 1000 K (Figure 7F).

4. DISCUSSION

4.1. The Role of Surface and Subsurface Diffusion in the Formation of TiO_x Decoration Adlayers on Rh Nanoparticles Supported by $\text{TiO}_2(110)$ Surface. The formation of epitaxial, ultrathin oxide layers on the top of metal nanoparticles supported on oxide surfaces is a result of a rather complex diffusion process in which the kinetic parameters of both the surface and subsurface diffusion are of importance.³⁷ Regarding the limited mass

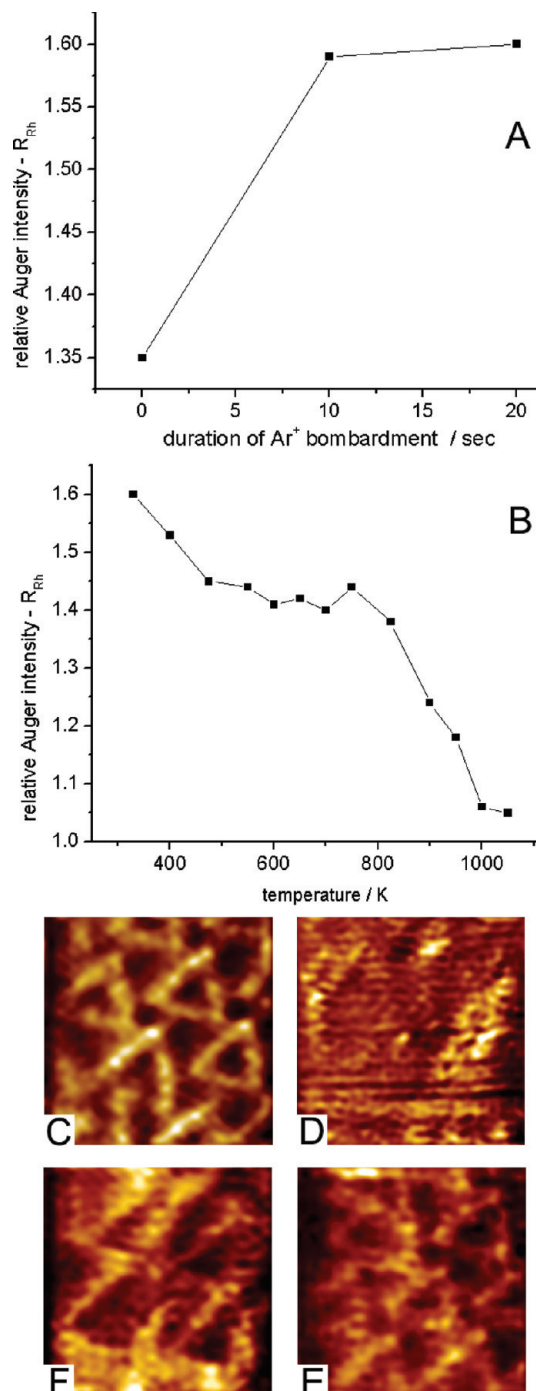


Figure 7. AES and STM detection of removal and restoration of ordered TiO_x decoration SMSI layer covering Rh nanoparticles. Change in the relative intensity of Rh(302 eV) and Ti(385 eV) AES signals as a function of (A) Ar^+ sputtering duration up to 20 s and (B) the subsequent annealing at elevated temperatures. The characteristic constant height STM images ($4 \times 4 \text{ nm}^2$) of the structure of top facets of Rh nanoparticles (C) before and after 20 s Ar^+ sputtering followed by annealing at (D) 650, (F) 900, and (E) 1000 K.

transport in the formation of an atomic scale adlayer and the diffusion distances of only few nanometers, we can assume that after the thermal treatment of several minutes at 900–1100 K, the energetically stable state can be reached for the decoration systems investigated here. Concerning the source of the mass

transport, the components of the support oxide structure should be mobile at the temperatures of the decoration process. It is known that the mobility of the metal and oxygen atoms is higher in the reduced oxide phases; accordingly, the formation of a decoration film takes place at lower temperatures on reduced $\text{TiO}_2(110)$ surfaces than on stoichiometric ones.^{3,37,43}

This feature also connects strongly to the original observation of SMSI, where the formation of this state was detected as a result of annealing in hydrogen atmosphere. It was assumed that the primary role of this gas is probably reducing the surface and subsurface region of the support.^{1,3} Note that the preliminary step for the SMSI process is the spillover of hot atomic hydrogen formed by the dissociation of H_2 molecules on the metal particle. The defect sites formed in this way in the surface and subsurface region of the oxide will serve as a diffusion path for the Ti and O atoms, although the role of the interstitial diffusion cannot be neglected.^{44–46} Moreover, the surface diffusion of certain atomic clusters of Ti_xO_y may also play some role, as was shown for the slightly sputtered $\text{TiO}_2(110)$ surfaces.⁴⁷

Fu and Wagner have called attention to the dual driving force of the decoration process: (i) interfacial charge redistribution (electronic interaction) and (ii) interfacial mass transport (chemical interaction).³⁷ Note that this duality is also expressed in the double designation ("strong metal–support interaction, SMSI" and "decoration"), which incidentally induced vigorous debates on the mechanism of the process. Actually, the "decoration" is mainly indicative of the mass transport, while the original meaning of SMSI is expressively related on the electronically influenced CO uptake.^{1,48} In their review, Fu and Wagner completed the mechanism of SMSI by proposing a strong interplay between the chemical and electronic effects. They emphasize the connection between the interfacial space charge and the diffusion of ionic defects across the interface.³⁷ In other words, the mass diffusion processes from the subsurface region to the surface are significantly activated by the charge distribution (Schottky barrier) determined by the work function of the constituent materials.

The diffusion of constituent metal ions of the oxide to the supported metal particles is not retarded effectively at the oxide–particle perimeter line because they bind more stably on the metal particles than on the support itself. This feature reveals itself in the fact that we have never detected extra material accumulated at the perimeter of the crystallites. At the same time, on filling up the decoration overlayer, this driving force will be drastically attenuated. This effect probably leads to the well-known self-limitation of the decoration layer, keeping it in atomically thin layer form.

The decoration oxide film toward the metal nanoparticle is usually terminated by the metal atom of the oxide due to the stronger bonding between M_{support} and M_{particle} than between O_{support} and M_{particle} . Accordingly, the characteristic decoration layers consist of M–O double layers terminated by O toward the vacuum, as in the case of the zigzag or wagon-wheel structures.^{6–8} This is probably also the case for the decoration layer formed on Rh nanoparticles supported on a $\text{TiO}_2(110)$ surface. Naturally, the stoichiometry of the decoration layer formed by a certain annealing treatment is determined by the oxidation state of the support and the particle/decoration interface energy. This condition results in a sensitive variation of the decoration layer composition, as was studied in detail for Pt/TiO_2 systems.^{11–15}

For a two-dimensional ordering of the accumulated oxide phase on the top facet of the supported metal nanocrystallite, several requirements have to be fulfilled: (i) a sufficiently large

(5–10 nm²) flat facet of the metal crystallite and (ii) a rather strong bond between the oxide ultrathin film and the metal or sufficiently large cohesion inside the layer of the 2D form, preventing its transformation into 3D oxide particles. The studies on the reactivity of encapsulated particles indicate that a complete capping layer (sheet) is rather unreactive toward adsorption of any gases. This is true even for not fully oxidized oxide layers;¹³ however, these complete ultrathin oxide films may play a very important role in different catalytic reactions.⁹

4.2. Comparison of "Wheel-Like" Decoration Layers

Found on Metal/Oxide Systems. The high-temperature, ultrathin oxide films exhibiting wheel-like (w) structure represent a characteristic and interesting long-range, ordered decoration phase that was observed for different oxide–metal compositions^{6,13,34,49–51} (Table 1). Note that the wheel-like arrangement is only a single case among the other ordered and quasi-ordered structures found and studied in detail; for example, the case of oxidative deposition of Ti onto Pt(111) surface.^{11–15}

Despite the overall similarity of w-structures, the details of their contrast and the interpretation of the pattern are yet unclear. The most important question is whether this film consists of only Ti and O or some mixing with the atoms of the supported noble metal, such as Rh and Pt, also takes place. The characteristic features of this arrangement depicted in Figure 8 are the following: (1) bright dots forming triangles, (2) three triangles constitute a wheel, (3) axle points of the wheels determine the unit cell, (4) the number of dots in the wheel spokes (part of the triangles), and (5) the characteristic distance between the neighboring dots. These data given for the different wheel structures are collected in Table 1.

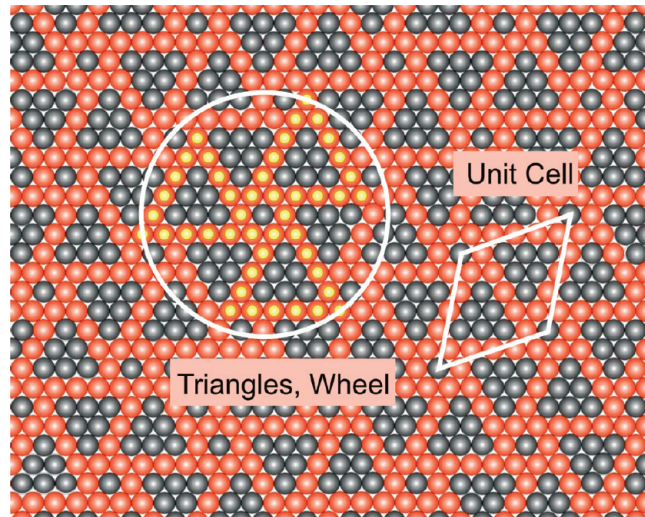
It is rather surprising that the clearest STM image for a w-structure was presented in the case of a Pt(111) surface exposed to Cr atoms at room temperature and annealed at 800 K without using oxygen.⁴⁸ The strong contrast of the wheel spokes was explained by the formation of a long-range ordered surface alloy in which the characteristic bright triangles consisted of Pt atoms. For this system, varying the bias direction caused a spectacular change in the STM contrast. Accepting this suggestion, Bowker and his co-workers interpreted the w-like decoration film formed on the top facets of Pd crystallites supported on TiO_2 as a surface alloy (Pd–Ti) oxide.⁶ In contrast to this explanation, the w-structure is identified as a two-dimensional M–O double layer in which the overlayer structure is terminated with oxygen atoms in the case of reactive deposition of Ti onto Pt(111) surface¹³ and that of V onto the Rh(111) surface.^{50,51} The large unit cell of this structure is probably the result of a slight misfit between the atomic lattice of the metal particles and that of the overlayer oxide (moiré pattern).

Table 1 reveals that the unit cell vector of these structures varies in the range of 1.5–1.9 nm and the number of spoke atoms changes in the range of 4–6. The assumption that the wheel structure is a moiré pattern implies also the statement that the supported oxide layer can be regarded as a sheet. Note that from this point of view, this thin film behaves similarly to the covalently bonded graphene. This condition is obviously much more fulfilled for the TiO_2 -film/Ru(0001) system, in which a clear moiré pattern appears.¹⁹ Nevertheless, the results shown in Table 1 refer to reduced a TiO_x film, for which the bonding to the supporting metal is probably more stable.

These conditions suggest double roots of appearance of the wheel pattern: (1) moiré-like behavior where the periodicity is determined by the lattice misfit and (2) significant lateral

Table 1. Wheel-Like Structures Detected for Different Oxide-Metal Systems

ref	overlayer and support	unit cell	spoke atoms, distance	layer content	general character	bias sens.	formation conditions
6, 34	decoration on hex. Pd particle supported by $\text{TiO}_2(110)$ (1×2)	hex. 1.50 nm	5 atom 0.34 nm	Pd–Ti oxidized alloy layer	str.wheel contrast		annealing at 700 K
49	Cr deposition on Pt(111)	$\sqrt{39} \times \sqrt{39}$ R16.1	6 atom	Cr–Pt alloy layer	str.wheel contrast	very strong	1.5–3 ML of Cr + annealing at 800 K
13	Ti deposition in oxygen on Pt(111)	hex. 1.73 nm	4 atom 0.34 nm	TiO layer with Pt–Ti–O structure	weak wheel contrast	strong	1.2 ML Ti in oxygen annealing at 823 K
13	Ti deposition in oxygen on Pt(111)	$\sqrt{43} \times \sqrt{43}$ R7.6	4 atom 0.34 nm	TiO layer with Pt–Ti–O structure	str.wheel contrast	strong	1.2 ML Ti in oxygen + annealing at 723 K
50, 51	V deposition in oxygen on Rh(111)	hex. 1.94 nm	6 atom 0.33 nm	cont. TiO layer Pt–Ti–O structure	str.wheel contrast	strong	1 ML V in oxygen + annealing at 700 K
this work	decoration hex. Rh partially on $\text{TiO}_2(110)$ (1×1) (1×2)	7×7 R21.8	6 atom 0.31 nm	VO inert layer Rh–V–O structure	strong wheel contrast	no	annealing at 900 K

**Figure 8. Scheme of the wheel structure.**

relaxation of the atoms in the oxide film caused by local interaction with the supporting metal atoms. In the case of Rh(111), the complex wheel structure is, in fact, a moiré pattern formed by a superposition of the hexagonal lattices of the oxide film with lattice constant of 0.31 nm and that of the underlying metal.

In the experiments presented in Figure 7, we tried to follow the building up of a wheel-like decoration layer. We assumed that the worm-like structure (Figure 3) consisting of 1D stripes (oriented in the close-packed direction of the Rh crystallites) is an initial state for the 2D wheel structure. Unfortunately, we did not find direct evidence, only a faint indication, for this idea. It is worth mentioning that the 1D type growth of ionically bonded layers on metal surfaces was found in several cases; for example, for sub-monolayer growth of NaCl on Cu(100).⁵² The uniform length of the TiO_x nanostripes observed in our case is probably caused by the accumulated strain appearing at their ends.

5. CONCLUSIONS

Formation of ordered decoration TiO_x layer was found on $\text{TiO}_2(110)$ -supported Rh nanoparticles as a result of annealing at 1050 K. This finding reveals that the formation of ordered 2D TiO_x films is a quite general feature for the noble metal/ TiO_2 systems. The encapsulation layer at saturation coverage exhibited a “wheel” structure with a hexagonal unit cell of ~ 1.5 nm \times 1.5 nm. The wheels are determined by three triangles consisting of 5 atoms in a distance of 0.31 nm. A “worm-like”, partially saturated layer was also detected which exhibited 1D stripes (nanostripes) oriented in the close-packed direction of the Rh(111) top facet. The characteristic sizes of these latter features are the following: width of 0.5 nm and length of 2–3 nm. The “worm-like” structure can be regarded as an initial state for the formation of the “wheel” arrangement. It was proved that it is possible to selectively remove the “wheel-like” decoration layer by Ar^+ sputtering (0.5 keV) and to subsequently restore it by a short thermal treatment at 1000 K.

■ ASSOCIATED CONTENT

S Supporting Information. Images showing the surface morphology at room temperature after the deposition of app.

1 ML of Rh at 850 K; after deposition of 5 ML of Rh at 1050 K; after 10 min annealing at 1050 K in vacuum. This material is available free of charge via the Internet at <http://pubs.acs.org>.

AUTHOR INFORMATION

Corresponding Author

*Phone: +36 62 544 646. Fax: +36 62 420 678. E-mail: aberko@chem.u-szeged.hu.

Present Addresses

^sDepartment of Thin Films, Institute of Physics of the Academy of Sciences of Czech Republic, Cukrovarnická 10, Prague 6, 162 53 Czech Republic.

ACKNOWLEDGMENT

We thank our colleagues, Dr. László Deák and Dr. László Óvári, for the fruitful discussions about the topic presented here. The authors also gratefully acknowledge the financial support provided by the Hungarian Scientific Research Fund (OTKA) through K69200 and K81660 projects.

REFERENCES

- (1) Tauster, S. J.; Fung, S. C. *J. Catal.* **1978**, *55*, 29–35.
- (2) Bowker, M.; Stone, P.; Bennett, R. A.; Perkins, N. *Surf. Sci.* **2002**, *497*, 155–165.
- (3) Berkó, A.; Ulrych, I.; Prince, K. C. *J. Phys. Chem. B* **1998**, *102*, 3379–3386.
- (4) Pesty, F.; Steinrück, H.-P.; Madey, Th. E. *Surf. Sci.* **1995**, *339*, 83–95.
- (5) Williams, K. J.; Salmeron, M.; Bell, A. T.; Somorjai, G. *Surf. Sci.* **1988**, *204*, L745–L753.
- (6) Bowker, M.; Stone, P.; Morrall, P.; Smith, R.; Bennett, R. A.; Perkins, N.; Kvon, R.; Pang, C.; Fourre, E.; Hall, M. *J. Catal.* **2005**, *234*, 172–181.
- (7) Jennison, D. R.; Dulub, O.; Hebestreit, W.; Diebold, U. *Surf. Sci.* **2001**, *492*, L677–L687.
- (8) Dulub, O.; Hebenstreit, W.; Diebold, U. *Phys. Rev. Lett.* **2000**, *84*, 3646–3649.
- (9) Sun, Y.-N.; Qin, Z.-H.; Lewandowski, M.; Carraco, E.; Sterrer, M.; Shaikhutdinov, S.; Freund, H.-J. *J. Catal.* **2009**, *266*, 359–368. Lewandowski, M.; Sun, Y. N.; Qin, Z.-H.; Shaikhutdinov, S.; Freund, H.-J. *Appl. Catal., A* **2011**, *391*, 407–410.
- (10) Chambers, S. A. *Surf. Sci. Rep.* **2000**, *39*, 105–180.
- (11) Boffa, A. B.; Galloway, H. C.; Jacobs, P. W.; Benítez, J. J.; Batteas, J. D.; Salmeron, M.; Bell, A. T.; Somorjai, G. A. *Surf. Sci.* **1995**, *326*, 80–92.
- (12) Barcaro, G.; Sedona, F.; Fortunelli, A.; Granozzi, G. *J. Phys. Chem. C* **2007**, *111*, 6095–6102.
- (13) Sedona, F.; Rizzi, G. A.; Agnoli, S.; Llabrés i Xamena, F. X.; Papageorgiou, A.; Ostermann, D.; Sambi, M.; Finetti, P.; Schierbaum, K.; Granozzi, G. *J. Phys. Chem. B* **2005**, *109*, 24411–244126.
- (14) Finetti, P.; Sedona, F.; Rizzi, G. A.; Mick, U.; Sutara, F.; Svec, M.; Matolin, V.; Schierbaum, K.; Granozzi, G. *J. Phys. Chem. C* **2007**, *111*, 869–876.
- (15) Zhang, Y.; Giordano, L.; Pacchioni, G.; Vittadini, A.; Sedona, F.; Finetti, P.; Granozzi, G. *Surf. Sci.* **2007**, *601*, 3488–3496.
- (16) Orzali, T.; Casarin, M.; Granozzi, G.; Sambi, M.; Vittadini, A. *Phys. Rev. Lett.* **2006**, *97*, 156101–156104.
- (17) Matsumoto, T.; Batzill, M.; Hsieh, S.; Koel, B. E. *Surf. Sci.* **2004**, *572*, 127–145.
- (18) Matsumoto, T.; Batzill, M.; Hsieh, H.; Koel, B. E. *Surf. Sci.* **2004**, *572*, 146–161.
- (19) Männig, A.; Zhao, Z.; Rosenthal, D.; Christmann, K.; Hoster, H.; Rauscher, H.; Behm, R. J. *Surf. Sci.* **2005**, *576*, 29–44.
- (20) Maeda, T.; Kobayashi, Y.; Kishi, K. *Surf. Sci.* **1999**, *436*, 249–258.
- (21) Passeggi, M. C. G., Jr.; Vergara, L. I.; Mendoza, S. M.; Ferrón, J. *Surf. Sci.* **2002**, *507*, 825–831.
- (22) Ashworth, T. V.; Thornton, G. *Thin Solid Films* **2001**, *400*, 43–45.
- (23) Ashworth, T. V.; Muryn, C. A.; Thornton, G. *Nanotechnology* **2005**, *16*, 3041–3044.
- (24) Chang, Z.; Thornton, G. *Surf. Sci.* **2000**, *462*, 68–76.
- (25) Atrei, A.; Bardi, U.; Rovida, G. *Surf. Sci.* **1997**, *391*, 216–225.
- (26) Biener, J.; Farfan-Arribas, E.; Biener, M.; Frienda, C. M.; Madix, R. J. *J. Chem. Phys.* **2005**, *123*, 94705–94711.
- (27) Rosenthal, D.; Zizak, I.; Darowski, N.; Magkoev, T. T.; Christmann, K. *Surf. Sci.* **2006**, *600*, 2830–2840.
- (28) Chen, M. S.; Goodman, D. W. *Science* **2004**, *306*, 252–255.
- (29) Chen, M. S.; Wallace, W. T.; Kumar, D.; Yan, Z.; Gath, K. K.; Cai, Y.; Kuroda, Y.; Goodman, D. W. *Surf. Sci.* **2005**, *581*, L115–L121.
- (30) Oh, W. S.; Xu, C.; Kim, D. Y.; Goodman, D. W. *J. Vac. Sci. Technol. A* **1997**, *15*, 1710–1716.
- (31) Guo, Q.; Oh, W. S.; Goodman, D. W. *Surf. Sci.* **1999**, *437*, 49–60.
- (32) Lai, X.; Guo, Q.; Min, B. K.; Goodman, D. W. *Surf. Sci.* **2001**, *487*, 1–8.
- (33) Herman, G. S.; Gallagher, M. C.; Joyce, S. A.; Peden, C. H. F. *J. Vac. Sci. Technol. B* **1996**, *14*, 1126–1130.
- (34) Bennett, R. A.; McCavish, R. D. *Top. Catal.* **2005**, *36*, 11–19.
- (35) McCavish, N. D.; Bennett, R. A. *Surf. Sci.* **2003**, *546*, 47–56.
- (36) Diebold, U. *Surf. Sci. Rep.* **2003**, *48*, 53–229.
- (37) Fu, Q.; Wagner, T. *Surf. Sci. Rep.* **2007**, *62*, 431–498.
- (38) Óvári, L.; Berkó, A.; Balázsz, N.; Majzik, Z.; Kiss, J. *Langmuir* **2010**, *26*, 2167–2175.
- (39) Berkó, A.; Solymosi, F. *Langmuir* **1996**, *12*, 1257–1261.
- (40) Berkó, A.; Solymosi, F. *Surf. Sci.* **1998**, *400*, 281–289.
- (41) Berkó, A.; Szökö, J.; Solymosi, F. *Solid State Ionics* **2001**, *141*–*142*, 197–202.
- (42) Berkó, A.; Hakkel, O.; Szökö, J.; Solymosi, F. *Surf. Sci.* **2002**, *507*–*510*, 643–648.
- (43) Bernal, S.; Botana, F. J.; Calvino, J. J.; Pérez-Omil, J. A.; Rodríguez-Izquierdo, J. M. *J. Chem. Soc. Faraday Trans.* **1996**, *92*, 2799–2809.
- (44) He, J.; Behera, R. K.; Finniss, M. W.; Li, X.; Dickey, E. C.; Phillipot, S. R.; Sinnott, S. B. *Acta Mater.* **2007**, *55*, 4325–4337.
- (45) Henderson, M. A. *Surf. Sci.* **1999**, *419*, 174–187.
- (46) Huntington, H. B.; Sullivan, G. A. *Phys. Rev. Lett.* **1965**, *14*, 177.
- (47) Berkó, A.; Bíró, T.; Kecskés, T.; Solymosi, F. *Vacuum* **2001**, *61*, 317–322.
- (48) Solymosi, F. *J. Catal.* **1985**, *94*, 581–585.
- (49) Zhang, L. P.; van Ek, J.; Diebold, U. *Phys. Rev. B* **1999**, *59*, 5837–5846.
- (50) Schoiswohl, J.; Sock, M.; Eck, S.; Surnev, S.; Ramsey, M. G.; Netzer, F. P.; Kresse, G. *Phys. Rev. B* **2004**, *69*, 155403–155416.
- (51) Schoiswohl, J.; Surnev, S.; Sock, M.; Eck, S.; Ramsey, M. G.; Netzer, F. P.; Kresse, G. *Phys. Rev. B* **2005**, *71*, 165437–165445.
- (52) Mauch, I.; Kaindl, G.; Bauer, A. *Surf. Sci.* **2003**, *522*, 27–33.